ORIGINAL RESEARCH PAPER
Pages: 109-125

Solution of 2-D Electromagnetic Problems for Inhomogeneous Objects using 1-D FFT

M. Parizi, M. Nakhkash
Electrical Engineering Dept., Yazd University, Yazd, Iran
mahdi.parizi@stu.yazd.ac.ir, nakhkash@yazd.ac.ir
Corresponding author: nakhkash@yazd.ac.ir

DOI:10.22070/jce.2021.13555.1175

***Abstract*- This paper presents a novel solution of two dimensional (2-D) method of moments (MoM) in Cartezian coordination to calculate the source-type electric field integral equations (EFIE) arising from electromagnetic inverse scattering problems in microwave imaging (MI). The main issue is to reduce the 2-D problem into 1-D case, using decomposition the electric-type Green's function of inhomogeneous media. In this regard, recursive formulas in spatial frequency domain are derived for both TE and TM problems and the scattering field is rewritten into upward and downward components in a recursive form. It helps us to calculate a 2-D problem using 1-D stabilized biconjugate-gradient fast Fourier transform (BCGSFFT) of the induced source and save lots of memory and time for inhomogeneous objects in MI performance. The paper provides 2-D TM and TE scattering examples for different scenarios and compares the proposed and conventional algorithms to demonstrate merits of the proposed formulas in terms of the accuracy and computational efficiency.**

***Index Terms*-** BCGSFFT, computational efficiency, EFIE, microwave imaging and scattering Problem.

I. INTRODUCTION

The diagnostic applications use different approches. Microwave imaging is one of the most important techniques, which aimed at sensing a given scene by means of interrogating microwaves. This active technique has proved capable of providing excellent diagnostic capabilities in several areas, including geophysical prospecting, remote sensing, civil and industrial engineering, nondestructive testing and evaluation (NDT & E), and biomedical engineering [1]-[14]. In this regard several different approaches can be applied. One of the most popular is inverse scattering – based procedure, which addresses the data inversion in several different ways depending on the target itself or on the imaging configuration and operation conditions [15]. The numerical methods for

Manuscript received 20-April-2020 and revised 5-June-2020,
Accepted on 27-June-2020
P- ISSN: 2322-4088
E- ISSN: 2322-3936

electromagnetic problems in the frequency domain involve the iterative solution of a source-type integral equation (IE) for known sources. Discretizing the problem geometry, the IE can be cast into matrix-vector product (MVP). By the virtue of convolutional nature of the IE, the FFT makes efficient implementation of the multiplication, requiring $O(N \log_2 N)$ arithmetic operations (where N is the number of unknowns) [16]-[17]. There are different approaches to deal with numerical scattering problems by decomposition involved functions (mostly green function) and derive novel formulas, decreasing time and computational complexity in MI performance [18].

The present paper introduces an efficient method to perform the MVP using 1-D FFT instead of 2-D version for 2-dimensional electromagnetic problems. The method is based on novel closed-form equations in *k*-space (spatial frequency domain), by which the scattered field can be calculated from the 1-D Fourier transform of the induced source. The resultant algorithm improves the computational efficiency for many cases, specially, when the background medium is lossy and/or the object has narrow width. Also, our algorithm presents good accuracy comparable to that of the conventional method (which employs 2-D FFT). The method is validated by comparisons with classical solutions for different scenarios and some 2-D TM and TE numerical examples are also given in order to show the applicability and the effectiveness.

II. PROBLEM FORMULATION

Consider the geometry of a 2-D electromagnetic problem shown in Fig. 1, where an inhomogeneous object with spatial support of D is located in a background medium with the permittivity ε_b, conductivity σ_b and permeability μ_b. The object has the spatially variable permittivity $\varepsilon(\mathbf{r})$, conductivity $\sigma(\mathbf{r})$ and a constant permeability $\mu = \mu_b$ (i.e. the object and the background medium have the same permeability). For TM problems, the total electric field at any point $\mathbf{r} = x\,\hat{x} + y\,\hat{y}$ satisfies

$$E_z^{\mathrm{t}}(\mathbf{r}) = E_z^i(\mathbf{r}) + E_z(\mathbf{r}) = E_z^i(\mathbf{r}) + k_b^2\, A_z(\mathbf{r}) \tag{1}$$

and for TE case, the field $\mathbf{E}(\mathbf{r}) = E_x(\mathbf{r})\,\hat{x} + E_y(\mathbf{r})\,\hat{y}$ is given by

$$\mathbf{E}^{\mathrm{t}}(\mathbf{r}) = \mathbf{E}^i(\mathbf{r}) + \mathbf{E}(\mathbf{r}) = \mathbf{E}^i(\mathbf{r}) + k_b^2 \mathbf{A}(\mathbf{r}) + \nabla\left[\nabla.\mathbf{A}(\mathbf{r})\right] \tag{2}$$

Let $E_q^{\mathrm{t}}(\mathbf{r})$, $E_q^i(\mathbf{r})$ and $E_q(\mathbf{r})$ are, respectively, q components of the total, incident and scattered fields (q can be x, y or z). The quantity $A_q(\mathbf{r})$ is equal to

$$A_q(\mathbf{r}) = \iint_D g(\mathbf{r},\mathbf{r}')\ \phi_q(\mathbf{r}')\ d^2\mathbf{r}',\ \phi_q(\mathbf{r}) = \chi(\mathbf{r})\, E_q^t(\mathbf{r}) \tag{3}$$

in which $g(\mathbf{r})$ is the scalar Green's function of the background medium and $\phi_q(\mathbf{r})$ denotes induced

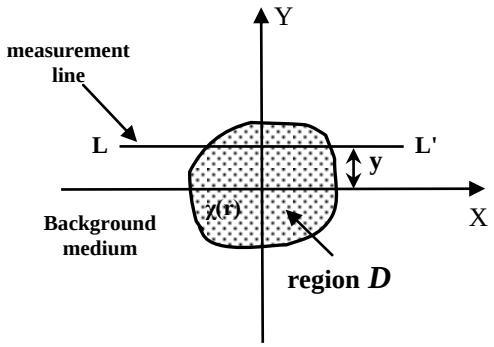

Fig. 1. The geometry of a 2-D electromagnetic problem.

source. With time dependence $\exp(j\omega t)$, $\chi(\mathbf{r}) = k^2(\mathbf{r})/k_b^2 - 1$ where $k_b^2 = \omega^2 \mu_b \varepsilon_b - j\omega\mu_b \sigma_b$ and $k^2(\mathbf{r}) = \omega^2 \mu_b \varepsilon(\mathbf{r}) - j\omega\mu_b \sigma(\mathbf{r})$.

In order to solve Eq. (1) or (2), the iterative algorithms need the computation of (3) for known $\phi_q(\mathbf{r})$ at every iteration. Let the object domain D be embedded in a rectangle $\Re$ that is discretized to $M_x \times N_y$ square cells and obtain (3) by the method of moment (MOM). With proper selection of testing and expansion functions in MOM, Eq. (3) is converted to MVP that is evaluated using 2-D FFT [1]. In this way, the total number of complex multiplications required for (3) would be

$$N_{2\text{DFFT}} = 8M_x N_y \log_2(4M_x N_y) + 4M_x N_y \tag{4}$$

The dominant factor determining the cost of computation is the first term of (4) for both TM and TE incident. Regarding operator $\nabla(\nabla.)$ in (2), different treatments have been accounted for its evaluation [19]-[20]. In all cases, they introduce minor contribution toward the expense of the computation.

III. NOVEL FORMULATION USING 1-D FOURIER TRANSFORM

The Green function for 2-D problems can be written as [21]

$$g(\mathbf{r},\mathbf{r}') = -\frac{j}{4} H_0^{(2)}(k_b|\mathbf{r}-\mathbf{r}'|) = -\frac{j}{4\pi}\int_{-\infty}^{+\infty} \exp[j\kappa(x-x')] \frac{\exp[-j\gamma|y-y'|]}{\gamma} d\kappa \tag{5}$$

in which $H_0^{(2)}$ is zero-order Hankel function of the second kind and $\gamma = \sqrt{k_b^2 - \kappa^2}$. Inserting (5) into (3), we have

$$A_q(x,y)=\frac{-j}{4\pi}\iint_D\left[\int_{-\infty}^{+\infty}\exp\left[j\kappa(x-x')\right]\times \frac{\exp\left[-j\gamma|y-y'|\right]}{\gamma}\,d\kappa\right]\phi_q(x',y')\;dx'dy' \tag{6}$$

Considering the line LL' in Fig. 1 is within region D, one can decompose $A_q(x,y)$ on this line to the upward wave $A_q^{\text{up}}(x,y)$ and downward wave $A_q^{\text{dn}}(x,y)$. For $y'\le y$, Eq. (6) gives $A_q^{\text{up}}(x,y)$ as

$$A_q^{up}(x,y)=\frac{-j}{4\pi}\iint_{D_{\text{up}}}\left[\int_{-\infty}^{+\infty}\exp\left[j\kappa(x-x')\right]\times \frac{\exp\left[j\gamma(y'-y)\right]}{\gamma}\,d\kappa\right]\phi_q(x',y')\;dx'dy' \tag{7}$$

where $D_{\text{up}}=\left\{(x',y')\in D\mid y'\le y\right\}$. Changing the integral order in (7) and taking 1-D Fourier transform with respect to x variable, one can derive

$$\tilde{A}_q^{\text{up}}(\kappa,y)=\left[-j\exp(-j\gamma\,y)\;\tilde{\phi}_q^{\text{up}}(\kappa,-\gamma)\right]/2\gamma \tag{8}$$

where $\tilde{A}_q^{\text{up}}$ denotes 1-D Fourier transform of the upward wave and $\tilde{\phi}_q^{\text{up}}(\kappa,\rho)$ denotes 2-D Fourier transform of the part of ϕ_q defined in D_{up} (κ and ρ are the spatial frequencies in x and y directions, respectively). In the same manner, defining $D_{\text{dn}}=\left\{(x',y')\in D\mid y'>y\right\}$, 1-D Fourier transform of the downward wave is obtained as

$$\tilde{A}_q^{\text{dn}}(\kappa,y)=\left[-j\exp(j\gamma\,y)\;\tilde{\phi}_q^{\text{dn}}(\kappa,\gamma)\right]/2\gamma \tag{9}$$

The above two equations relate 1-D Fourier transform of $A_q(x,y)=A_q^{\text{up}}(x,y)+A_q^{\text{dn}}(x,y)$ to 2-D Fourier transform of the induced source. It is possible to extract relations in terms of 1-D Fourier transfer of ϕ_q from (8) and (9). Consider embedding region $\Re$ is defined as the rectangle $\Re=\left\{(x',y')\mid x_1\le x'\le x_2\ ,\ y_1\le y'\le y_2\right\}$. One can write for $\tilde{\phi}_q^{\text{up}}(\kappa,\rho)$

$$\tilde{\phi}_q^{\text{up}}(\kappa,\rho)=\int_{x_1}^{x_2}\int_{y_1}^{y}\phi_q(x',y')\exp(-jy'\rho)\,\exp(-jx'\kappa)\;dy'dx'=$$
$$\sum_{n=N_1}^{N-1}\int_{x_1}^{x_2}\exp(-jx'\kappa)\left[\int_{(n-1/2)\Delta}^{(n+1/2)\Delta}\phi_q(x',y')\,\exp(-jy'\rho)\;dy'\right]dx'+ \tag{10}$$
$$\int_{x_1}^{x_2}\exp(-jx'\kappa)\left[\int_{(N-1/2)\Delta}^{y}\phi_q(x',y')\,\exp(-jy'\rho)\;dy'\right]dx'$$

where $y_1=(N_1-1/2)\Delta$ and $(N-1/2)\Delta\le y<(N+1/2)\Delta$. If Δ is enough small, the induced

field does not vary, significantly, in interval $\left[(n-1/2)\Delta,\ (n+1/2)\Delta\right]$ and we may use the approximation $\phi_q(x',y')=\phi_q(x',n\Delta)$ in this interval. Therefore, the evaluation of the inner integrals (inside [ ]) in (10) and the substitution of resultant $\tilde{\phi}_q^{\,\mathrm{up}}(\kappa,\rho)$ in (8) gives

$$\tilde{A}_q^{\mathrm{up}}(\kappa,y)=\frac{-j}{\gamma^2}\sin\left(\gamma\frac{\Delta}{2}\right)\exp(-j\gamma y)\sum_{n=N_1}^{N-1}\tilde{\phi}_q(\kappa,n\Delta)\exp(j\gamma n\Delta)\ +$$
$$\frac{1}{2\gamma^2}\left[\exp(-j\gamma y)\ \exp\left(j\gamma(N-1/2)\Delta\right)-1\right]\tilde{\phi}_q(\kappa,N\Delta) \tag{11}$$

in which $\tilde{\phi}_q(\kappa,n\Delta)$ is 1-D Fourier transform of $\phi_q(x',n\Delta)$ in x direction. When $y_2=(N_2+1/2)\Delta$ and $(N-1/2)\Delta<y\le(N+1/2)\Delta$, the same procedure for the downward wave provides

$$\tilde{A}_q^{\mathrm{dn}}(\kappa,y)=$$
$$\frac{-j}{\gamma^2}\sin\left(\gamma\frac{\Delta}{2}\right)\exp(j\gamma y)\sum_{n=N+1}^{N_2}\tilde{\phi}_q(\kappa,n\Delta)\exp(-j\gamma n\Delta)\ +$$
$$\frac{1}{2\gamma^2}\left[\exp(j\gamma y)\ \exp\left(-j\gamma(N+1/2)\Delta\right)-1\right]\tilde{\phi}_q(\kappa,N\Delta) \tag{12}$$

We use Equations (11) and (12) to derive recursive formulas for TM and TE incident.

A. Recursive Formulation for TM Problem

The substitution of $y=N\Delta$ in (11) yields $\tilde{A}_z^{\mathrm{up}}(N)=\tilde{A}_z^{\mathrm{up}}(\kappa,N\Delta)$ from which $\tilde{A}_z^{\mathrm{up}}(N-1)$ may be found and then doing some manipulation, one can derive

$$\tilde{A}_z^{\mathrm{up}}(N)=\tilde{R}(\kappa,\Delta)\,\tilde{A}_z^{\mathrm{up}}(N-1)+\tilde{S}(\kappa)\,\tilde{\phi}_z(N-1)+\tilde{T}(\kappa)\,\tilde{\phi}_z(N) \tag{13}$$

where $\tilde{\phi}_z(n)=\tilde{\phi}_z(\kappa,n\Delta)$ and

$$\tilde{R}(\kappa,y)=\exp(-j\gamma y)\ ,\ \tilde{T}(\kappa)=\frac{1}{2\gamma^2}\left[\exp(-j\gamma\Delta/2)-1\right]$$
$$\tilde{S}(\kappa)=\frac{1}{2\gamma^2}\left[\exp(-j\gamma\Delta)-\exp\left(-j\gamma\Delta/2\right)\right] \tag{14}$$

Equation (13), recursively, relates 1-D Fourier transform of the upward wave on the line $N\Delta$ (inside the object region) to those on and below this line. Similarly, we have

$$\tilde{A}_z^{\mathrm{dn}}(N)=\tilde{R}(\kappa,\Delta)\ \tilde{A}_z^{\mathrm{dn}}(N+1)+\tilde{S}(\kappa)\ \tilde{\phi}_z(N+1)+\tilde{T}(\kappa)\ \tilde{\phi}_z(N) \tag{15}$$

According to (13) and (15), the computation of (1) for known ϕ_z involves taking 1-D Fourier transform of the induced source on horizontal lines in the rectangle $\Re$ and, then, use (13) and (15) to

obtain the total field E_z on these lines. Equations (13) and (15) can be implemented discretely and one way is to sample $\tilde{R}(\kappa,\Delta)$, $\tilde{S}(\kappa)$ and $\tilde{T}(\kappa)$ in *k*-space at the points imposed from FFT of the induced source. Nevertheless, this method may yield considerable error in spatial domain (*x* direction) because the sampling in *k*-space gives rise to aliasing in the spatial domain. Another way is to derive the discrete form of (13) and (15) in the spatial domain by dividing the x axis to Δ intervals. For instance, we consider the third multiplicative term in (13) and (15), which is converted to convolution in x domain. Denoting F^{-1} as the inverse Fourier transform, $A_T(x,N\Delta)=F^{-1}[\tilde{T}(\kappa)\ \tilde{\phi}_z(N)]$ is given by

$$A_T(x,N\Delta)=\sum_{m=M_1}^{M_2}\int_{(m-1/2)\Delta}^{(m+1/2)\Delta}\phi_z(x',N\Delta)\,T(x-x')\,dx' \tag{16}$$

where we set $x_1=(M_1-1/2)\Delta$ and $x_2=(M_2+1/2)\Delta$ in embedding region $\Re$. Since Δ is sufficiently small, ϕ_z is essentially constant over each interval. Thus enforcing (16) at the center of interval M (i.e. $x=M\Delta$) and denoting $A_T(M,N)=A_T(M\Delta,N\Delta)$, $\phi_z(m,N)=\phi_z(m\Delta,N\Delta)$, the following expression is obtained

$$A_T(M,N)=\sum_{m=M_1}^{M_2}\phi_z(m,N)\ T_I(M-m) \tag{17}$$

in which $T_I(m)=\int_{(m-1/2)\Delta}^{(m+1/2)\Delta}T(x')\,dx'$. Taking the same procedure for the second and first terms in (13) and (15) and let $A_S(x,N\Delta)=F^{-1}[\tilde{S}(\kappa)\ \tilde{\phi}_z(N)]$ and $A_R^{\mathrm{wv}}(x,N\Delta)=F^{-1}[\tilde{R}(\kappa,\Delta)\ \tilde{A}_z^{\mathrm{wv}}(N)]$ (wv is up or dn), one may derive

$$A_S(M,N)=A_S(M\Delta,N\Delta)=\sum_{m=M_1}^{M_2}\phi_z(m,N)\ S_I(M-m) \tag{18}$$

$$A_R^{\mathrm{wv}}(M,N)=A_R^{\mathrm{wv}}(M\Delta,N\Delta)=\sum_{m=-\infty}^{+\infty}A_z^{\mathrm{wv}}(m,N)\,R_I(M-m,\Delta) \tag{19}$$

Equations (17), (18) and (19) are in form of 1-D discrete convolutions that can be, efficiently, implemented by FFT. Appendix A derives a closed-form expression for the sequences $T_I(m)$ and $S_I(m)$; but $R_I(m,\Delta)$ is found by numerical integration.

The sequence $\phi_z(m,N)$ in (17) and (18) is finite size, i.e. $M_1\le m\le M_2$. Thus, the exact implementation of (17) and (18) is possible by expanding $\phi_z(m,N)$ to $2(M_2-M_1)=2M_x$ points by zero padding and using FFT. However, neither $A_z^{\mathrm{wv}}(m,N)$ nor $R_I(m,\Delta)$ is finite to compute (19), similarly. Equation (A7) shows sequence $R_I(m,\Delta)$ is the integral of derivative of Green

function over $[(m-1/2)\Delta,(m+1/2)\Delta]$. Consequently, this sequence, rapidly, approaches zero as m is increased and it may, approximately, truncate to a finite sequence. The problem arisen from such a truncation is the recursion in (13), which makes $\tilde{A}_z^{\text{up}}(N_1)$ at $y'_1 = N_1\,\Delta$ (the bottom line of $\Re$) be multiplied by $\tilde{R}^{(N_2-N_1)}(\kappa,\Delta)=\exp\left[-j\gamma(y'_2-y'_1)\right]$ to obtain $\tilde{A}_z^{\text{up}}(N_2)$ at $y'_2 = N_2\,\Delta$ (the top line of $\Re$). The same argument is true for $\tilde{A}_z^{\text{dn}}$ as well. The length of truncation should, therefore, be obtained with respect to decay speed of $R(x,y'_2-y'_1)=F^{-1}\left\{\exp\left[-j\gamma(y'_2-y'_1)\right]\right\}$ that is less than that of $R(x,\Delta)$. In order to specify the truncation length x_t, we apply a criterion on energy of $R(x,y'_2-y'_1)$ as follows

$$\int_0^{x_t}\left|R(x',y'_2-y'_1)\right|^2 dx' \geq \xi\int_{x_t}^{\infty}\left|R(x',y'_2-y'_1)\right|^2 dx' \qquad (20)$$

where $\xi>1$. Using (20), Appendix B gives $x_t = M_t\,\Delta$ for two cases of lossless and lossy background media.

Regarding the above explanations, the algorithm prescription to obtain scattered field in (1) is as follows: the sequences $T_I(m)$, $S_I(m)$ and $R_I(m,\Delta)$ are computed at $2(M_x+M_t)$ points and $\phi_z(m,N)$ is zero padded to expand it to the same number of points; Then, calculating FFT of these sequences, the discrete versions of (13) and (15) are implemented. There are N_y sequences $\phi_z(m,N)$, whose 1-D FFT requires total $2N_y(M_x+M_t)\log_2\left[2(M_x+M_t)\right]$ complex multiplications and the same number of operations is needed to obtain inverse FFT of $\tilde{A}_z(N)=\tilde{A}_z^{\text{up}}(N)+\tilde{A}_z^{\text{dn}}(N)$. The computation of the each term in (13) or (15) requires $2N_y(M_x+M_t)$ complex operations and considering the (13) and (15) share the calculation of the second and third terms, the total operations would be $8N_y(M_x+M_t)$. Therefore, the computational cost for calculation of A_z in (1) gives rise to

$$N_{1DFFT} = 4N_y(M_x+M_t)\log_2\left[2(M_x+M_t)\right]+8N_y(M_x+M_t) \qquad (21)$$

Comparison of (21) and (4) reveals the use of Eq. (13) and (15) could improve efficiency if M_t keeps under a limit. Appendix B (relations (B4), (B5) and (B7)) indicates M_t is descending function of σ_b (or generally loss tangent $\sigma_b/\omega\varepsilon_b$ of the background medium) and ascending function of N_y (i.e. the thickness y_2-y_1 of region $\Re$). As a result, the computational efficiency is enhanced for narrow embedding regions $\Re$ ($N_y<M_x$) and/or lossy background media.

B. Recursive Formulation for TE Problem

The 1-D Fourier transform of the scattering field in (2) with respect to x yields

$$\begin{aligned}\tilde{E}_x(\kappa, y) &= \gamma^2\, \tilde{A}_x(\kappa, y) + j\kappa \frac{\partial \tilde{A}_y(\kappa, y)}{\partial y} \\ \tilde{E}_y(\kappa, y) &= k_b^2\, \tilde{A}_y(\kappa, y) + \frac{\partial^2 \tilde{A}_y(\kappa, y)}{\partial y^2} + j\kappa \frac{\partial \tilde{A}_x(\kappa, y)}{\partial y}\end{aligned} \tag{22}$$

Using (11) in (22) and putting $y = N\Delta$, we get $\tilde{E}_q^{\text{up}}(N) = \tilde{E}_q^{\text{up}}(\kappa, N\Delta)$. Then, if $\tilde{E}_q^{\text{up}}(N-1)$ is found, the recursive relations for TE problem will be

$$\begin{aligned}\tilde{E}_x^{\text{up}}(N) &= \tilde{R}(\kappa,\Delta)\,\tilde{E}_x^{\text{up}}(N-1) + \left[\tilde{R}(\kappa,\Delta) - \tilde{R}(\kappa,\Delta/2)\right]\tilde{\phi}_x(N-1)/2 + \\ &\quad \left[\tilde{R}(\kappa,\Delta/2) - 1\right]\tilde{\phi}_x(N)/2 + \tilde{W}(\kappa)\,[\tilde{\phi}_y(N) - \tilde{\phi}_y(N-1)] \\ \tilde{E}_y^{\text{up}}(N) &= \tilde{R}(\kappa,\Delta)\,\tilde{E}_y^{\text{up}}(N-1) + \left[\tilde{R}(\kappa,\Delta/2)/2 + k_b^2\,\tilde{S}(\kappa)\right]\tilde{\phi}_y(N-1) + \\ &\quad \left[k_b^2\,\tilde{T}(\kappa) - \tilde{R}(\kappa,\Delta/2)/2\right]\tilde{\phi}_y(N) + \tilde{W}(\kappa)\,[\tilde{\phi}_x(N) - \tilde{\phi}_x(N-1)]\end{aligned} \tag{23}$$

in which $\tilde{R}(\kappa, y)$, $\tilde{S}(\kappa)$ and $\tilde{T}(\kappa)$ are given in (14) and $\tilde{W}(\kappa) = \dfrac{\kappa}{2\gamma}\exp(-j\gamma\,\Delta/2)$. For downward wave, one can, similarly, obtain

$$\begin{aligned}\tilde{E}_x^{\text{dn}}(N) &= \tilde{R}(\kappa,\Delta)\,\tilde{E}_x^{\text{dn}}(N+1) + \left[\tilde{R}(\kappa,\Delta) - \tilde{R}(\kappa,\Delta/2)\right]\tilde{\phi}_x(N+1)/2 + \\ &\quad \left[\tilde{R}(\kappa,\Delta/2) - 1\right]\tilde{\phi}_x(N)/2 + \tilde{W}(\kappa)\,[\tilde{\phi}_y(N+1) - \tilde{\phi}_y(N)] \\ \tilde{E}_y^{\text{dn}}(N) &= \tilde{R}(\kappa,\Delta)\,\tilde{E}_y^{\text{dn}}(N+1) + \left[\tilde{R}(\kappa,\Delta/2)/2 + k_b^2\,\tilde{S}(\kappa)\right]\tilde{\phi}_y(N+1) + \\ &\quad \left[k_b^2\,\tilde{T}(\kappa) - \tilde{R}(\kappa,\Delta/2)/2\right]\tilde{\phi}_y(N) + \tilde{W}(\kappa)\,[\tilde{\phi}_x(N+1) - \tilde{\phi}_x(N)]\end{aligned} \tag{24}$$

The discussion for the discrete implementation of (13) and (15) can be, equally, applied to Eq. (23) and (24). Consequently, we require the sequences $S_I(m)$, $T_I(m)$, $R_I(m,\Delta)$, $R_I(m,\Delta/2)$ (dealt in Appendix A) and sequence $W_I(m) = \int_{(m-1/2)\Delta}^{(m+1/2)\Delta} W(x')\,dx'$. Considering $W(x)$ is derivative of $g(x,y)$ (i.e. A1) with respect to x, $W_I(m)$ is exactly obtained as

$$W_I(m) = \frac{-j}{4}\left\{H_0^{(2)}\left[k_b\,\Delta\sqrt{(m+0.5)^2 + 0.25}\right] - H_0^{(2)}\left[k_b\,\Delta\sqrt{(m-0.5)^2 + 0.25}\right]\right\} \tag{25}$$

The computational cost for TE problems would be, nearly, twice of (21). That is because there are two field components.

IV. NUMERICAL EXAMPLES

This section provides several examples to demonstrate the merits of the proposed recursive formulas and compare its application with that of the conventional formula. The stabilized

biconjugate-gradient FFT (BCGSFFT) [16] is used to solve 2-D TM and TE scattering problems. The scattered field is obtained for known induced source at each iteration of BCGSFFT using conventional 2-D FFT and the novel 1-D FFT formulas, referring the combination as BCGSFFT2D and BCGSFFT1D methods, respectively. The BCGSFFT2D is implemented in accordance with [1] to compute A_q by 2-D FFT, and then, utilize the central finite differencing [20] to calculate $\nabla(\nabla.)$ operator if the problem is TE.

The incident field is a unit amplitude plane wave with z component for TM case and with x component for TE case, traveling in y direction. The permeability μ_b is equal to μ_0 (free-space permeability), the discretization width Δ is set to 5 mm, and parameter ξ in criterion (20) acquires value 5 in all examples. The iteration process in BCGSFFT is terminated when relative residual error Err satisfies the following criterion

$$Err = \left\| L(\mathbf{E}) - \mathbf{E}^{inc} \right\| / \left\| \mathbf{E}^{inc} \right\| \leq 0.01 \tag{26}$$

where $\| \|$ denotes L_2-norm and $L[E_z(\mathbf{r})] = E_z(\mathbf{r}) - k_b^2 A_z(\mathbf{r})$ for TM incident and $L[\mathbf{E}(\mathbf{r})] = \mathbf{E}(\mathbf{r}) - k_b^2 \mathbf{A}(\mathbf{r}) - \nabla[\nabla.\mathbf{A}(\mathbf{r})]$ for TE incident. Because of stopping rule (26), the number of iterations for BCGSFFT2D (N_{Ite}^{2D}) and BCGSFFT1D (N_{Ite}^{1D}) algorithms can be different and, therefore, the ratio $N_{Ite}^{2D} / N_{Ite}^{1D}$ is provided to compare the convergent speed of two algorithms. The improvement in the computational efficiency can be judged according to the efficiency gain that is the ratio of numbers given by (4) and (21), i.e. $G_{eff} = N_{2DFFT} / N_{1DFFT}$.

We, first, apply BCGSFFT2D and BCGSFFT1D to 2-D problems with circular scatterers, for which the analytical solution is available and can serve as a reference to obtain the accuracy of the methods. The quantitative measure of accuracy is the relative error defined as

$$e_r^{\text{alg}} = \left\| \mathbf{E}^{\text{anal}} - \mathbf{E}^{\text{alg}} \right\| / \left\| \mathbf{E}^{\text{anal}} \right\| \tag{27}$$

Field $\mathbf{E}^{\text{anal}}$ is the scattered field yielded by the analytical solution and $\mathbf{E}^{\text{alg}}$ indicates the scattered field from either BCGSFFT2D (alg = 2D) or BCGSFFT1D (alg = 1D). Tables 1 and 2 list the results for different scenarios. Note that ε_{rb} and ε_r denotes the relative permittivity of the background medium and the object, respectively, and d is the diameter of the circular objects.

For TM incident, it can be observed the BCGSFFT2D presents better accuracy, especially for lossless media. Although the accuracy of BCGSFFT1D may be increased if ξ in (20) acquires large values, our experiences show that the accuracy improvement needs the significant deterioration of the efficiency. As σ_b becomes larger, the BCGSFFT1D provides more accurate results, which is because

Table 1: The accuracy and efficiency of BCGSFFT2D and BCGSFFT1D methods for $\varepsilon_{rb}=1, \sigma_b=0$

		$\varepsilon_r=4,\ \sigma=0,\ d=20\,\text{cm}$		$\varepsilon_r=8,\ \sigma=50\,\text{mS/m}, d=40\,\text{cm}$	
Frequency (MHz)		500	2000	500	2000
TM	e_r^{2D}	0.0109	0.0582	0.0028	0.0412
	e_r^{1D}	0.0916	0.0655	0.0309	0.0753
	$N_{Ite}^{2D}/N_{Ite}^{1D}$	1.00	1.03	1.00	1.24
	G_{eff}	1.08	1.08	1.13	1.13
TE	e_r^{2D}	0.0924	0.1436	0.0604	0.3113
	e_r^{1D}	0.1106	0.1309	0.0627	0.2177
	$N_{Ite}^{2D}/N_{Ite}^{1D}$	1.25	1.04	1.00	0.97
	G_{eff}	1.05	1.05	1.10	1.10

Table 2: The performance of BCGSFFT2D and BCGSFFT1D for $\varepsilon_{rb}=4, \sigma_b=500\,\text{mS/m}$

		$\varepsilon_r=4,\ \sigma=0,\ d=20\,\text{cm}$		$\varepsilon_r=8,\ \sigma=50\,\text{mS/m}, d=40\,\text{cm}$	
Frequency (MHz)		500	2000	500	2000
TM	e_r^{2D}	0.0247	0.0580	0.0217	0.0735
	e_r^{1D}	0.0565	0.0780	0.0282	0.1121
	$N_{Ite}^{2D}/N_{Ite}^{1D}$	1.00	1.00	1.00	1.00
	G_{eff}	1.62	1.70	1.82	1.90
TE	e_r^{2D}	0.1521	0.0787	0.0655	0.0879
	e_r^{1D}	0.1283	0.0674	0.0702	0.1196
	$N_{Ite}^{2D}/N_{Ite}^{1D}$	0.89	0.91	1.00	1.33
	G_{eff}	1.59	1.65	1.77	1.84

$R_I(m,\Delta)$ resembles better a finite sequence. The results of TE incident indicate the both methods have more or less the same accuracy, though BCGSFFT1D becomes superior for some cases. We speculate this is due to the exact treatment of $\nabla(\nabla.)$ operator in *k*-space to derive the recursive formulas (23) and (24). Considering the true efficiency gain is $G_{eff}\times N_{Ite}^{2D}/N_{Ite}^{1D}$, the tables indicate the computational cost of BCGSFFT1D is less than BCGSFFT2D for the examples satisfying $N_y=M_x\geq 40$ and $\xi=5$. The larger is the problem (large N_y and M_x), the more efficient is BCGSFFT1D algorithm. It is pointed out in Subsection III.A the computational efficiency of

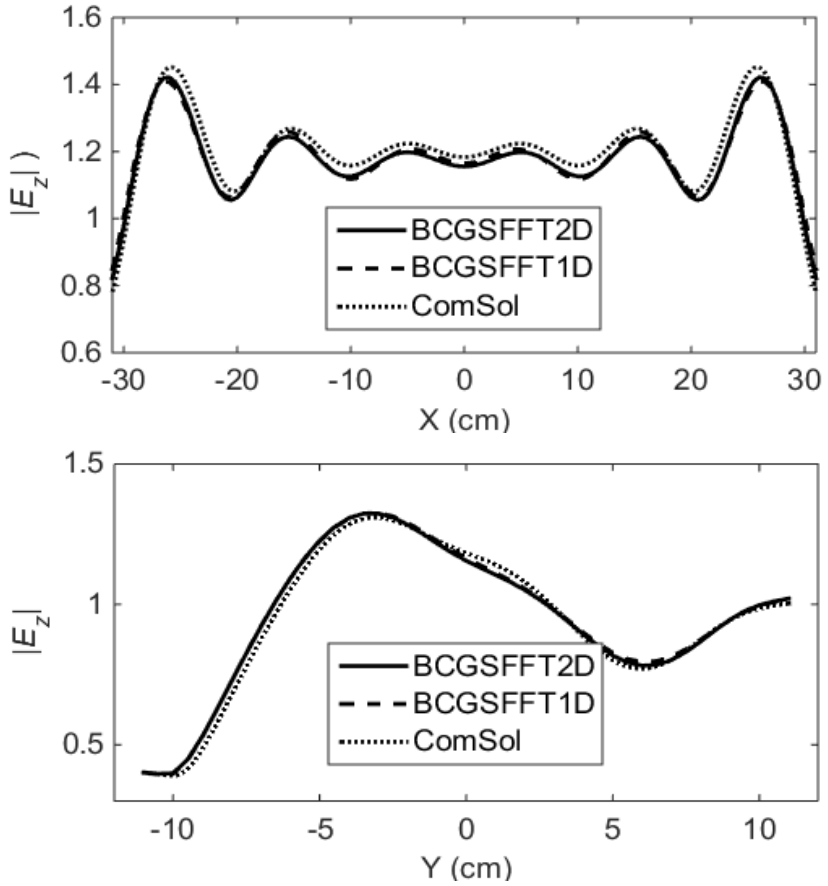

Fig. 2. The scattered fields of a rectangle for TM incident at 1500 MHz. The sides of the rectangle in x and y directions are 60cm and 20cm and it has $\varepsilon_r = 5, \sigma = 100$ mS/m with the background $\varepsilon_{rb} = 1, \sigma_b = 0$. The performance parameters are $e_1^{1D} = 0.0388$, $e_r^{2D} = 0.0374$, $N_{Ite}^{2D} / N_{Ite}^{1D} = 0.96$ and $G_{eff} = 1.81$.

BCGSFFT1D is enhanced when the background medium becomes lossy. The tables confirm the efficiency is ascending function of background losses (σ_b).

Equation (B7) implies the improvement of BCGSFFT1D efficiency for narrow embedding regions $\Re$ (i.e. $N_y < M_x$). To demonstrate this, we obtain the field scattered from a solid rectangular object having 60 cm side in x direction and 20 cm side in y direction. It has the parameters $\varepsilon_r = 5, \sigma = 100$ mS/m and the background medium is free space ($\varepsilon_{rb} = 1$, $\sigma_b = 0$). Since the analytical solution for rectangles is not available, we use the results from ComSol software as a reference to judge the accuracy for this example. The TM results of BCGSFFT2D and BCGSFFT1D and simulation results with ComSol at 1500 MHz are compared in Fig. 2, where the magnitude of the scattered field is shown at the center of the rectangle in x and y directions. The closeness of the

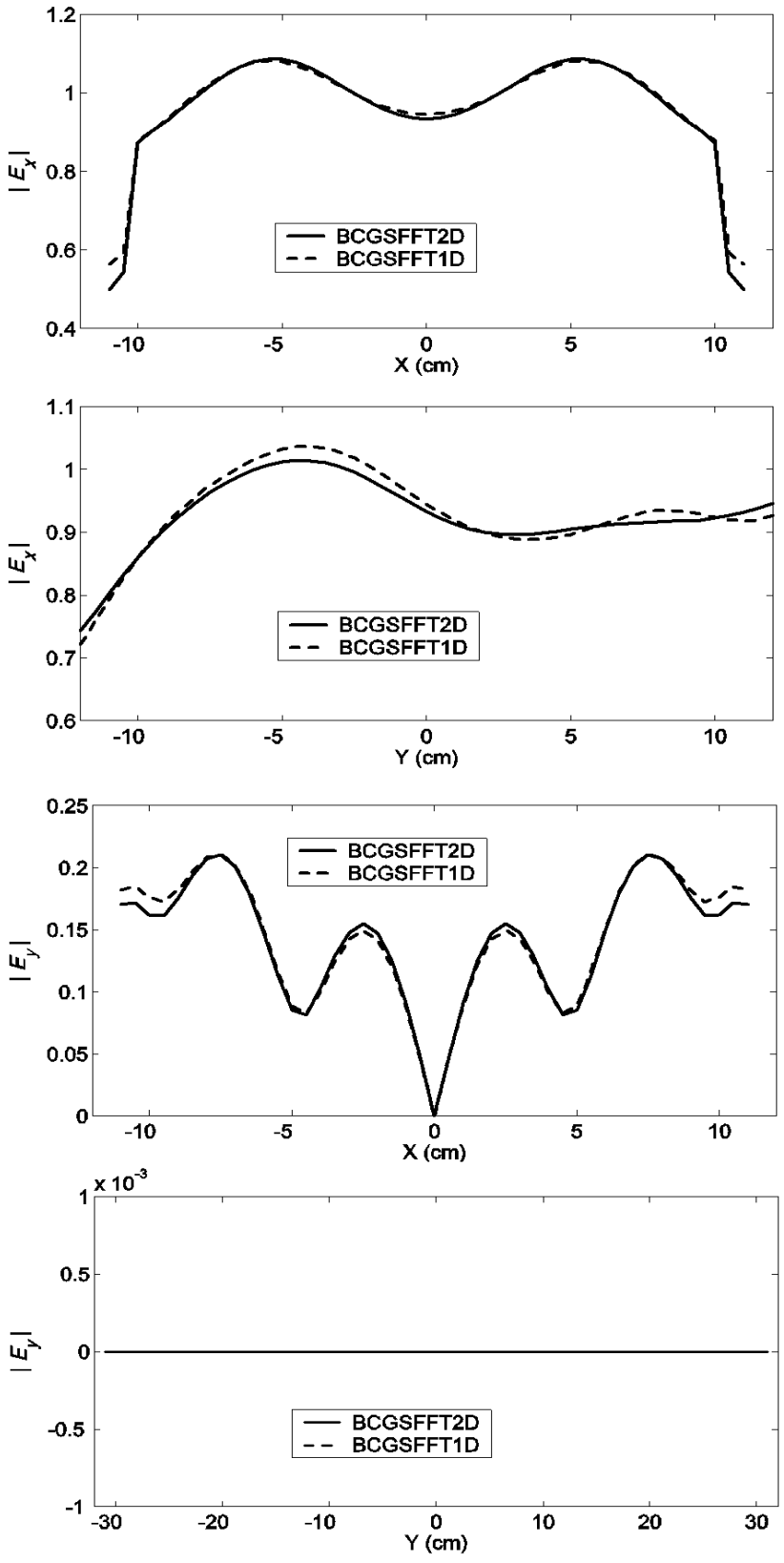

Fig. 3. The illustration of applying the novel method to 90° rotated version of the rectangle described in Fig. 2 for TE incident. Performance parameters are $e_r = 0.0635$, $N_{Ite}^{2D} / N_{Ite}^{1D} = 0.96$ and $G_{eff} = 1.75$.

results is quantified by $e_r^{alg} = \left\| \mathbf{E}^{comsol} - \mathbf{E}^{alg} \right\| / \left\| \mathbf{E}^{comsol} \right\|$ in analogy with (27). Fig. 2 illustrates good resemblance of the resultant fields of the methods. Regarding the computational efficiency, the simulations are carried out for two limiting squares of $20\text{cm}\times 20\text{cm}$ and $60\text{cm}\times 60\text{cm}$, having the same electromagnetic parameters as the aforementioned rectangle. The relative accuracy is obtained according to $e_r = \left\| \mathbf{E}^{2D} - \mathbf{E}^{1D} \right\| / \left\| \mathbf{E}^{2D} \right\|$. The performance parameters are as follows:

$20\text{cm}\times 20\text{cm}$ Square: $e_r = 0.0260$ $\quad$ $60\text{cm}\times 60\text{cm}$ Square: $e_r = 0.0126$

$N_{Ite}^{2D} / N_{Ite}^{1D} = 1.00$, $G_{eff} = 1.08$ $\quad$ $N_{Ite}^{2D} / N_{Ite}^{1D} = 0.90$, $G_{eff} = 1.16$

Comparing the results of Fig. 2 with the above, it can be concluded that narrowing the object (region $\Re$) improves the efficiency of BCGSFFT1D over BCGSFFT2D. The efficiency of our novel method is enhanced even if $\Re$ is narrow in y direction as well. Under such condition, BCGSFFT1D acts on the object rotated 90° (note that the incident wave is, correspondingly, rotated). Using BCGSFFT1D method this way, Fig. 3 shows the outcomes of 90° rotated version of the previous rectangle (i.e. a rectangle having 20 cm side in x and 60 cm side in y directions). It is evident the improvement of BCGSFFT1D efficiency is achieved even for narrow $\Re$ in y direction.

V. DISCUSSION AND CONCLUSION

To solve 2-D scattering problems using 1-D FFT, novel recursive formulas have been derived. For lossy background media and TE problems, numerical examples illustrate the use of the new formulas provides a comparative accuracy in contrast to the conventional method employing 2-D FFT. When the background medium is lossless and dealing with TM problems, the usage of the recursive formulas introduces less accuracy, which could be tolerated in many practical applications.

The theoretical and numerical results show that the computational efficiency of our novel formulas is enhanced with the increase of background medium loss, narrowing any side of embedding region ($N_y \neq M_x$) and expansion of the problem scale. To have a quantitative view of the efficiency gain, (B7) suggests $M_t = \eta N_y$ that gives

$$G_{eff} = \frac{2M_x \log_2(4M_x N_y) + M_x}{(M_x + \eta N_y)\left\{\log_2\left[2(M_x + \eta N_y)\right] + 2\right\}} \tag{28}$$

If region $\Re$ is square ($M_x = N_y = K$), (28) is simplified to

$$G_{eff} = \frac{4\log_2(2K) + 1}{(1+\eta)\left\{\log_2\left[2(1+\eta)K\right] + 2\right\}} \tag{29}$$

Setting $\xi = 5$ and being the background lossless, Eq. (29) concludes $G_{eff} > 1$ if $K > 15$. Clearly, the efficiency gain would be larger for lossy background and/or when the minimum of M_x and N_y is greater than 15. That means the recursive formulas have efficiency superiority over the conventional method for all practical cases. In case the background medium poses significant losses (i.e. $\eta \to 0$) and the problem is large scale, G_{eff} attains value 4. These all justify the use of our proposed formulas.

For the case of 3-D problems, Green function may be represented by [21]

$$g(\mathbf{r},\mathbf{r}') = \frac{\exp(-j k_b |\mathbf{r}-\mathbf{r}'|)}{4\pi|\mathbf{r}-\mathbf{r}'|} = -\frac{j}{8\pi^2}\iint \exp\left[j\left(k_x(x-x')+k_y(y-y')\right)\right] \times \frac{\exp\left[-j\gamma|z-z'|\right]}{\gamma} dk_x\, dk_y \tag{30}$$

Therefore, one can take the same procedure in this paper and derive a method that solves 3-D electromagnetic problems using 2-D FFT instead of 3-D FFT.

APPENDEX A. 1-D CONVOLUTIONAL FUNCTIONS

According to (5), the Green function for $y \geq 0$ can be written as

$$g(x,y) = -\frac{j}{4\pi}\int_{-\infty}^{+\infty} \exp[j\kappa x]\frac{\exp[-j\gamma y]}{\gamma} d\kappa \tag{A1}$$

The integral of $g(x,y)$ in terms of y within interval $[0, \Delta/2]$ results in

$$T(x) = \frac{1}{2\pi}\int_{-\infty}^{+\infty} \exp(j\kappa x)\ \frac{1}{2\gamma^2}\left[\exp(-j\gamma\frac{\Delta}{2}) - 1\right] d\kappa \tag{A2}$$

that is inverse Fourier of $\tilde{T}(\kappa)$ as it is concluded from Eq. (14). Being $g(x,y)$ an even function with respect to x and y, $T_I(m)$ is given by

$$T_I(m) = \int_{(m-1/2)\Delta}^{(m+1/2)\Delta} T(x)\, dx = \frac{1}{2}\int_{(m-1/2)\Delta}^{(m+1/2)\Delta}\int_{-\Delta/2}^{\Delta/2} g(x,y)\, dy\, dx \tag{A3}$$

The above double integral has equivalent volume solution as [22]

$$T_I(m) = \begin{cases} \dfrac{-j\sqrt{\pi}\,\Delta}{4k_b}\, H_1^{(2)}\left(k_b\dfrac{\Delta}{\sqrt{\pi}}\right) - \dfrac{1}{2k_b^2} & , \quad m = 0 \\ \dfrac{-j\sqrt{\pi}\,\Delta}{4k_b}\, J_1\left(k_b\dfrac{\Delta}{\sqrt{\pi}}\right) H_0^{(2)}(m k_b \Delta) & , \quad m \neq 0 \end{cases} \tag{A4}$$

where J_1 and $H_1^{(2)}$ are order one Bessel function and Hankel function of the second kind respectively. We may, also, drive

$$S(x)=\int_{\Delta/2}^{\Delta} g(x,y)\,dy=\int_{0}^{\Delta} g(x,y)\,dy-\int_{0}^{\Delta/2} g(x,y)\,dy \tag{A5}$$

which results in

$$S_I(m)=\frac{-j\sqrt{\pi}\Delta}{2k_b}J_1\left(\frac{k_b\Delta}{\sqrt{\pi}}\right)H_0^{(2)}\left(k_b\,\Delta\sqrt{m^2+\frac{1}{4}}\right)-T_I(m) \tag{A6}$$

Taking the derivative of (A1) with regard to y, we have

$$R(x,y)=F^{-1}\left[\exp(-j\gamma y)\right]=\frac{-j\,k_b\,y}{2r}\,H_1^{(2)}\left(k_b\,r\right) \tag{A7}$$

where $r=|\mathbf{r}|=\sqrt{x^2+y^2}$. The integral $R_I(m,y)=\int_{(m-1/2)\Delta}^{(m+1/2)\Delta}R(x,y)\,dx$ cannot be found analytically. Thus, the numerical integration, such as adaptive Simpson quadrature, is employed to compute $R_I(m,y)$.

APPENDEX B. EVALUATION OF THE TRUNCATION LENGTH

The solution of inequality (20) yields the truncation length x_t. Using the large argument form of $H_1^{(2)}$, it follows from (A7)

$$R(x,y)=\frac{-j\,k_b\,y}{2r}\sqrt{\frac{2}{\pi\,k_b\,r}}\,\exp\left[-j\left(k_b\,r-3\pi/4\right)\right] \tag{B1}$$

Setting $y=y'_2-y'_1$, the large argument approximate is valid because $k_b r\ge k_b(y'_2-y'_1)$ and $k_b(y'_2-y'_1)$ is large for many problems. The substitution of (B1) into the criterion (20) provides

$$\int_0^{x_t}\frac{\exp(-2k_I\,r)}{r^3}\,dx\ge\xi\int_{x_t}^{+\infty}\frac{\exp(-2k_I\,r)}{r^3}\,dx \tag{B2}$$

where k_I denotes the imaginary part of $-k_b$. Changing variable from x to $r=\sqrt{x^2+y^2}$ (that gives $r_t=\sqrt{x_t^2+y^2}$) and integrating by part, the left side of (B2) becomes

$$I_1=\frac{\sqrt{r_t^2-y^2}}{y^2\,r_t}\exp(-2k_I r_t)+\frac{2k_I}{y^2}\int_y^{r_t}\frac{\sqrt{r^2-y^2}}{r}\exp(-2k_I r)\,dr \tag{B3}$$

The term $\exp(-2k_I\,r)$ in the right integral of (B3) acquires its minimum at $r=r_t$, i.e. $I_1\ge I_{1\min}$ so that

$$I_{1\min}=\left\{\frac{\sqrt{r_t^2-y^2}}{y^2\,r_t}+\frac{2k_I}{y^2}\left[\sqrt{r_t^2-y^2}-y\,\sec^{-1}\left(\frac{r_t}{y}\right)\right]\right\}\times\exp(-2k_I\,r_t) \tag{B4}$$

With regard to (B3), one may obtain the following limit for the right integral of (B2) denoted by I_2.

$$I_2 \le I_{2\max} \ , \ I_{2\max} = \left[1 - \frac{\sqrt{r_t^2 - y^2}}{r_t} \right] \frac{\exp(-2 k_I \, r_t)}{y^2} \tag{B5}$$

The inequality $I_{1\min} \ge \xi I_{2\max}$ clearly implies the inequality (B2). Let $u = r_t / y$, the equality $I_{1\min} = \xi I_{2\max}$ results in

$$(1+\xi) \sqrt{u^2 - 1} + 2 k_I \, y \, u \, [\sqrt{u^2 - 1} - \sec^{-1} u] - \xi u = 0 \tag{B6}$$

In case the background medium is lossless ($k_I = 0$), the inequalities (B4) and (B5) becomes equalities, i.e. the integrals in both side of (B2) can be precisely obtained, and we have $u_{lossless} = (1+\xi) / \sqrt{1+2\xi}$ that is the solution of equal part in inequality (B2). Generally, the root u of (B6) should be obtained by root finding algorithms like Newton method. Looking into (B5) and (B6), the increase of k_I reduces r_t to meet $I_{1\min} = \xi I_{2\max}$ and, hence, the root of (B6) would be in interval $[1, u_{lossless}]$. After the evaluation of u, the truncation length is obtained as $x_t = (y'_2 - y'_1) \sqrt{u^2 - 1}$ and the division by Δ yields

$$M_t = \mathrm{ceil}[N_y \sqrt{u^2 - 1}] \tag{B7}$$

where $\mathrm{ceil}(x)$ indicates the smallest integer value greater than x.

REFERENCES

[1] Q. H. Liu, Z. Q. Zhang, T. T. Wand, J. A. Bryan, G. A. Ybarra, L. W. Nolte, and W. T. Joines, "Active microwave maging. I. 2-D forward and inverse scattering methods," *IEEE Trans. Microwave Theory Tech*., vol. 50, no. 1, pp. 123-133, Jan. 2002.

[2] M. Salucci, G. Oliveri and A. Massa, "GPR prospecting through an inverse scattering frequency-hopping multi-focusing approach," *IEEE Trans. Geosci. Remote Sens*, vol. 53, no. 12, pp. 6573-6592, Dec. 2015.

[3] H. Zhang, J. Meng, L, Sun, X, Zhang and S, Shu, "Performance Analysis of Internal Solitary Wave Detection and Identification Based on Compact Polarimetric SAR," *IEEE Access*, vol. 8, pp. 172839-172847, Sep. 2020.

[4] M. Salucci, L. Poli, N. Anselmi and A. Massa, "Multi-frequency particle swarm optimization for enhanced multiresolution GPR microwave imaging," *IEEE Trans. Geosci. Remote Sens.*, vol. 55, no. 3, pp. 1305-1317, March 2017.

[5] F. Sabzevari, R. Winter, D, Oloumi and K. Rambabu, "A Microwave Sensing and Imaging Method for Multiphase Flow Metering of Crude Oil Pipes," *IEEE Journal of Selected Topics in Applied Earth Observations and Remote Sensing*, vol. 13, pp. 1286-1297, Mar. 2020.

[6] S. Kharkovsky, A.C. Ryley, V. Stephen and R. Zoughi, "Dual-polarized near-field microwave reflectometer for noninvasive inspection of carbon fiber reinforced polymer-strengthened structures," *IEEE Trans. Instrum. Meas*, vol. 57, no.1, pp.168-175, Jan. 2008.

[7] P. Giri and S. Kharkovsky, "Dual-laser integrated microwave imaging system for nondestructive testing of construction materials and structures," *IEEE Trans. Instrumentation and Measurement*, vol. 67, no. 6, pp. 1329-1337, June 2018.

[8] S.J. Liu, Z.Y. Xu, J.L. Wei et al., "Experimental study on microwave radiation from deforming and fracturing rock," *IEEE Geosci. Remote Sens*, vol. 54, no. 9, pp. 5578-5587, Sept. 2016.

[9] A. Massa et al., "A microwave imaging method for NDE/NDT based on the SMW technique for the electromagnetic field prediction," *IEEE Trans. Instrumentation and Measurement*, vol. 55, no. 1, pp. 240-147, Feb. 2006.

[10] J. T. Case, M. T. Ghasr and R. Zoughi, "Nonuniform Manual Scanning for Rapid Microwave Nondestructive Evaluation Imaging," *IEEE Trans. Instrumentation and Measurement*, vol. 62, no. 5, pp. 1250-1258, May 2013.

[11] T. D. Carrigan, B. E. Forrest, H. N. Andem, K. Gui, L. Johnson, J. E. Hibbert, et al., "Nondestructive testing of nonmetallic pipelines using microwave reflectometry on an in-line inspection robot," *IEEE Trans. Instrumentation and Measurement.*, vol. 68, no. 2, pp. 586-594, Feb. 2019.

[12] R. K. Amineh, M. Ravan and R. Sharma, "Nondestructive Testing of Nonmetallic Pipes Using Wideband Microwave Measurements," *IEEE Trans. Microwave Theory and Techniques*, vol. 68, no. 5, pp. 1763-1772, May 2020.

[13] M. Rahman, A. Haryono, Z. Akhter and M. Abou-Khousa "On the Inspection of Glass Reinforced Epoxy Pipes using Microwave NDT," *IEEE Intern. Instrumentation and Measurement Technology Conference (I2MTC)*, May 2019.

[14] T. Gholipur, M. Nakhkash, "A data focusing method for microwave imaging of extended targets," *Journal of Communication Engineering*, vol. 7, no. 1, Jan.-June 2018.

[15] M. Pastorino, *Microwave Imaging*, New York: Wiley, 2010,ch 4, pp. 57-78.

[16] X. M. Xu, Q. H. Liu and Z. Q. Zhang, "The stabilized biconjugate gradient fast Fourier transform method for electromagnetic scattering," *Appl. Computational Electromagnetic Soc. Jour.*, vol. 17, pp. 97-103, 2002.

[17] N. Joachimowicz, C. Pichot and J.P. Hugonin, "Inverse scattering: an iterative numerical method for electromagnetic imaging," *IEEE Trans. Antennas Propag.*, vol. 39, no. 12, pp. 1742-1753, Dec. 1991.

[18] E. Konakyeri Arıcı and A. Yapar, "Numerical Calculation of 2-D Inhomogeneous Media Green's Function and Some Applications in Electromagnetic Scattering Problems," *IEEE Trans. Antennas Propag.*, vol. 67 , no. 1, pp. 369-377, Jan. 2019.

[19] Z. Q. Zhang and Q. H. Liu, "Three-dimensional weak-form conjugate and biconjugate-gradient FFT methods for volume integral equations," *Microwave Opt. Technol. Lett.*, vol. 29, no. 5, pp. 350-356, June 2001.

[20] Z. Q. Zhang, Q. H. Liu, C. Xiao, E. Ward, G. Ybarra and W. T. Joines, "Microwave breast imaging: 3-D forward scattering simulation," *IEEE Trans. Biomedical Eng.*, vol. 50, no. 10, pp. 1180-1189, Oct. 2003.

[21] W. C. Chew, *Waves and Fields in Inhomogeneous Media*, Wiley-IEEE Press, New York, 1999.

[22] G. Gao, C. Torres-Verdin and T. M. Habashy, "Analytical techniques to evaluate the integrals of 3D and 2D spatial dyadic Green's functions," *Prog. Electromag. Research (PIER)*, vol. 52, pp. 47-80, 2005.